Magnetomotive contrast for *in vivo* optical coherence tomography

Amy L. Oldenburg

Department of Electrical and Computer Engineering, Beckman Institute for Advanced Science and Technology, University of Illinois at Urbana-Champaign, 405 N. Mathews Ave, Urbana, IL 61801, USA
oldenbrg@uiuc.edu

Farah Jean-Jacques Toublan and Kenneth S. Suslick

School of Chemical Sciences, Beckman Institute for Advanced Science and Technology, University of Illinois at Urbana-Champaign, 600 S. Mathews Ave, Urbana, IL 61801, USA
jeanjacq@uiuc.edu, ksuslick@uiuc.edu

Alexander Wei

Department of Chemistry, Purdue University, 560 Oval Dr., West Lafayette, IN 47907, USA
alexwei@purdue.edu

Stephen A. Boppart

Departments of Electrical and Computer Engineering, Bioengineering, Beckman Institute for Advanced Science and Technology, University of Illinois at Urbana-Champaign, 405 N. Mathews Ave, Urbana, IL 61801, USA
boppart@uiuc.edu

Abstract: Molecularly-specific contrast can greatly enhance the biomedical utility of optical coherence tomography (OCT). We describe a contrast mechanism, magnetomotive OCT (MMOCT), where a modulated magnetic field induces motion of magnetic nanoparticles. The motion of the nanoparticles modifies the amplitude of the OCT interferogram. High specificity is achieved by subtracting the background fluctuations of the specimen, and sensitivity to 220 μg/g magnetite nanoparticles is demonstrated. Optically and mechanically correct tissue phantoms elucidate the relationships between imaging contrast and nanoparticle concentration, imaging depth, tissue optical scattering, and magnetic field strength. MMOCT is demonstrated in a living *Xenopus laevis* tadpole where the results were consistent with corresponding histology.

OCIS codes: (170.4500) Optical coherence tomography; (160.3820) Magneto-optical materials; (290.5850) Scattering, particles

References and Links

1. D. Huang, E. A. Swanson, C. P. Lin, J. S. Schuman, W. G. Stinson, W. Chang, M. R. Hee, T. Flotte, K. Gregory, C. A. Puliafito, and J. G. Fujimoto, "Optical coherence tomography," Science **254**, 1178 (1991).
2. Y. Jiang, I. Tornov, Y. Wang, and Z. Chen, "Second-harmonic optical coherence tomography," Opt. Lett. **29**, 1090 (2004).
3. D. L. Marks and S. A. Boppart, "Nonlinear interferometric vibrational imaging," Phys. Rev. Lett. **92**, 123905 (2004).
4. C. Vinegoni, J. S. Bredfeldt, D. L. Marks, and S. A. Boppart, "Nonlinear optical contrast enhancement for optical coherence tomography," Opt. Express **12**, 331 (2004), http://www.opticsexpress.org/abstract.cfm?URI=OPEX-12-2-331
5. J. S. Bredfeldt, C. Vinegoni, D. L. Marks, and S. A. Boppart, "Molecularly sensitive optical coherence tomography," Opt. Lett. **30**, 495 (2005).
6. C. Loo, A. Lin, L. Hirsch, M.-H. Lee, J. Barton, N. Halas, J. West, and R. Drezek, "Nanoshell-enabled photonics-based imaging and therapy of cancer," Technol. Cancer Res. Treat. **3**, 33 (2004).

#8043 - $15.00 USD Received 6 July 2005; revised 15 August 2005; accepted 15 August 2005

7. T.-M. Lee, A. L. Oldenburg, S. Sitafalwalla, D. L. Marks, W. Luo, F. Jean-Jacques Toublan, K. S. Suslick, and S. A. Boppart, "Engineered microsphere contrast agents for optical coherence tomography," Opt. Lett. **28**, 1546 (2003).
8. U. Morgner, W. Drexler, F. X. Kartner, X. D. Li, C. Pitris, E. P. Ippen, and J. G. Fujimoto, "Spectroscopic optical coherence tomography," Opt. Lett. **25**, 111 (2000).
9. D. J. Faber, E. G. Mik, M. C. G. Aalders, and T. G. van Leeuwen, "Light absorption of (oxy-)hemoglobin assessed by spectroscopic optical coherence tomography," Opt. Lett. **28**, 1436 (2003).
10. C. Xu, J. Ye, D. L. Marks, and S. A. Boppart, "Near-infrared dyes as contrast-enhancing agents for spectroscopic optical coherence tomography," Opt. Lett. **29**, 1647 (2004).
11. C. Yang, L. E. L. McGuckin, J. D. Simon, M. A. Choma, B. E. Applegate, and J. A. Izatt, "Spectral triangulation molecular contrast optical coherence tomography with indocyanine green as the contrast agent," Opt. Lett. **29**, 2016 (2004).
12. K. D. Rao, M. A. Choma, S. Yazdanfar, A. M. Rollins, and J. A. Izatt, "Molecular contrast in optical coherence tomography by use of a pump-probe technique," Opt. Lett. **28**, 340 (2003).
13. C. Yang, M. A. Choma, L. E. Lamb, J. D. Simon, and J. A. Izatt, "Protein-based molecular contrast optical coherence tomography with phytochrome as the contrast agent," Opt. Lett. **29**, 1396 (2004).
14. H. Watarai and M. Namba, "Capillary magnetophoresis of human blood cells and their magnetophoretic trapping in a flow system," J. Chromatogr. A **961**, 3 (2002).
15. S. Palmacci and L. Josephson, "Synthesis of polysaccharaide covered superparamagnetic oxide colloids," United States Patent #5,262,176 (1993).
16. M. G. Harisinghani, J. Barentsz, P. F. Hahn, W. M. Deserno, S. Tabatabaei, C. Hulsbergen van de Kaa, J. de la Rosette, and R. Weissleder, "Noninvasive detection of clinically occult lymph-node metastases in prostate cancer," N. Engl. J. Med. **348**, 2491 (2003).
17. A. S. Arbab, G. T. Yocum, L. B. Wilson, A. Parwana, E. K. Jordan, H. Kalish, and J. A. Frank, "Comparison of transfection agents in forming complexes with ferumoxides, cell labeling efficiency, and cellular viability," Mol. Imaging **3**, 24 (2004).
18. A. L. Oldenburg, J. R. Gunther, and S. A. Boppart, "Imaging magnetically labeled cells with magnetomotive optical coherence tomography," Opt. Lett. **30,** 747 (2005).
19. J. W. Goodman, *Statistical Optics* (John Wiley & Sons, 1985).
20. U. Hafeli, W. Schutt, J. Teller, and M. Zborowski, *Scientific and Clinical Applications of Magnetic Carriers* (Plenum Press, 1997).
21. J. M. Schmitt, "Restoration of optical coherence images of living tissue using the CLEAN algorithm," J. Biomed. Opt. **3**, 66 (1998).
22. M. Pircher, E. Gotzinger, R. Leitgeb, A. F. Fercher, and C. K. Hitzenberger, "Speckle reduction in optical coherence tomography by frequency compounding," J. Biomed. Opt. **8**, 565 (2003).
23. G. Yao, L. V. Wang, "Signal dependence and noise source in ultrasound-modulated optical tomography," Appl. Opt. **43**, 1320 (2004).
24. S. Hamaguchi, I. Tohnai, A. Ito, K. Mitsudo, T. Shigetomi, M. Ito, H. Honda, T. Kobayashi, and M. Ueda, “Selective hyperthermia using magnetoliposomes to target cervical lymph node metastasis in a rabbit tongue tumor model,” Cancer Sci. **94**, 834 (2003).
25. A. L. Oldenburg, J. R. Gunther, F. Jean-Jacques Toublan, D. L. Marks, K. S. Suslick, and S. A. Boppart, "Selective OCT imaging of cells using magnetically-modulated optical contrast agents," in *Proceedings of the Conference on Lasers and Electro-Optics*, pp. 405-406 (2003).
26. M. Wojtkowski, V. J. Srinvasan, T. H. Ko, J. G. Fujimoto, A. Kowalczyk, and J. S. Duker, "Ultrahigh-resolution, high-speed, Fourier domain optical coherence tomography and methods for dispersion compensation," Opt. Express **12**, 2404 (2004), http://www.opticsexpress.org/abstract.cfm?URI=OPEX-12-11-2404
27. T. L Troy and S. N. Thennadil, "Optical properties of human skin in the near infrared wavelength range of 1000 to 2200 nm," J. Biomed. Opt. **6**, 167 (2001).
28. J. Schmitt, "OCT elastography: imaging microscopic deformation and strain of tissue," Opt. Express **3**, 199 (1998), http://www.opticsexpress.org/abstract.cfm?URI=OPEX-3-6-199
29. D. C. Cannatella and R. O. De Sa, "*Xenopus laevis* as a model organism," Syst. Biol. **42**, 476 (1993).
30. G. Bernardini, M. Prati, E. Boneti, and G. Scari, *Atlas of Xenopus Development* (Springer, 1999).

1. Introduction

Optical coherence tomography (OCT) is a non-invasive, micron resolution, biomedical imaging modality [1] with clinical application in several areas including ophthalmology, gastroenterology, and cardiology. Essentially a method of *in vivo* optical biopsy, OCT would greatly benefit from the availability of molecularly-specific markers to aid in real-time diagnosis or surgical guidance. Although this is analogous to the use of fluorescent stains in microscopy and histopathology, OCT cannot detect inelastically scattered light such as that emitted from fluorophores because such light is not coherent with respect to the incident field. Currently, higher-order elastic scattering mechanisms such as second harmonic generation [2]

#8043 - $15.00 USD Received 6 July 2005; revised 15 August 2005; accepted 15 August 2005

and coherent anti-Stokes Raman scattering [3-5] are being explored as sources of endogenous tissue contrast, where OCT-style interferometry is employed for depth-resolved imaging.

Recently there has been much interest in the development of synergistic contrast agents and contrast mechanisms appropriate for molecular contrast in OCT. Plasmon-resonant gold nanoshells [6] have been proposed as OCT contrast agents due to their high scattering cross-section. Liquid-core protein microspheres incorporating gold nanoparticles in their shells [7] also exhibit a large scattering efficiency and produce *in vivo* contrast within a mouse liver. Such passive scattering agents are disadvantageous in that they require *a priori* knowledge of the object structure in order to locate them amongst scattering tissue structures. Spectroscopic OCT, originally proposed as a means of producing endogenous tissue contrast [8,9], has been used to specifically locate near-infrared absorbing dyes [10,11] exhibiting distinctive wavelength-dependent absorption efficiencies. In general, spectroscopic analysis of OCT images is limited by degradation of the longitudinal resolution, which is inversely proportional to the spectral resolution ($\Delta\lambda$) required to detect the agents. Additional specificity against tissue background structures has been investigated using transient [12] or switchable absorption [13] in a dye molecule, which is then detected through difference imaging.

The interest in magnetic agents lies in the ability to externally control them with a magnetic field after their application to the tissue. Because tissue is not ferromagnetic and only weakly magnetic (*e.g.*, the magnetic volume susceptibility of water $\chi \sim -10^{-5}$ and hemoglobin in blood cells $|\chi| < 10^{-5}$ [14]), contrast agents such as magnetite (Fe_3O_4, $\chi \sim 1$) may be imaged with a large dynamic range using an interaction which exploits this disparity in χ. In fact, superparamagnetic iron oxide nanoparticles (SPIOs) with $\chi \approx 1$ are already FDA-approved as contrast agents for MRI [15]. Because macrophage cells readily uptake SPIOs, they have been utilized in clinical trials to identify metastatic lymph nodes which lack healthy macrophages [16]. The toxicity and uptake of iron oxide particles have been investigated with stem cells *in vitro*, where uptake of ~20 pg/cell of iron oxide did not significantly decrease cell proliferation [17].

In this work we describe and demonstrate a novel technique for imaging magnetic agents using OCT. Contrast is produced through the motive response of magnetic particles to an external field and the resulting locoregional changes to the optical scattering. Previous investigation using magnetomotive OCT (MMOCT) [18] indicates the ability to identify magnetically-labeled macrophage cells within a three-dimensional tissue scaffold. In this work we have improved upon the technique by using an acquisition scheme that samples the intrinsic background fluctuations to eliminate ghosting in the MMOCT images. Because the particles used here are nanoscale and thus sub-resolution, we cannot resolve them individually, but rather detect their aggregate response and how they displace structures (*e.g.* cells and organelles) within their microenvironment. As described below, we have employed optically and mechanically equivalent tissue phantoms to study the sensitivity, depth dependence, and dynamic range of MMOCT, as well as to investigate the underlying mechanics of how the MMOCT signal scales with the magnetic field, average tissue scattering amplitude, and magnetic particle concentration. Quantifying these parameters in a homogenous sample is a crucial first step toward producing calibrated concentration maps of targeted nanoparticles within structured tissues. Finally, we show that MMOCT is practical for *in vivo* imaging by identifying regions of higher (but non-toxic) magnetic particle concentrations within a living *Xenopus laevis* tadpole and matching these results with corresponding histology.

2. Theory

2.1 Definition of the Magnetomotive OCT Signal

There exist an abundance of physical mechanisms which may be exploited to provide a magnetomotive optical effect for optical contrast imaging. Particles exhibiting high magnetic susceptibility may be pulled in the direction of a strong magnetic field gradient. Elongated

#8043 - $15.00 USD Received 6 July 2005; revised 15 August 2005; accepted 15 August 2005

magnetic particles may be rotated in a magnetic field (either through remanence in ferromagnetic materials, or through shape anisotropy) which changes their scattering cross-section, and produces polarization-dependent scattering. These forces and torques on individual nanoparticles apply stresses within the viscoelastic biological medium, resulting in a speckle change observable in the OCT image. The primary consideration to producing magnetomotive contrast is to ensure the magnetically-induced speckle change is of larger magnitude, or otherwise separable through its statistical properties, from the speckle fluctuations intrinsic to the medium in the absence of magnetic excitation.

In practice we find a minimum of three measurements are necessary to provide both background and excitation data at each point $\vec{r}$ in the object: $a_{off}(t)$, $a_{off}(t+\Delta t)$, and $a_{on}(t+2\Delta t)$, where the subscripts "on" and "off" indicate the state of the magnetic field, and Δt is the time delay between measurements. Here we define a as the magnitude of the complex analytic signal derived via the Hilbert transform of the OCT interferogram. (The choice of tracking amplitude changes, and not the phase, is motivated by available hardware: it should be noted that phase modulation might also be an attractive metric for magnetomotive OCT.) The first two measurements sample the structure function D_{aoff} [19], which is a measure of the intrinsic background fluctuations:

$$\left\langle \left(a_{off}(t+\Delta t)-a_{off}(t)\right)^2 \right\rangle = D_{a_{off}}(\Delta t) = 2\left(\overline{a_{off}{}^2} - \Gamma_{a_{off}}(\Delta t)\right) \tag{1}$$

where we assume Brownian and other biological motions within the sample are wide-sense stationary. The autocorrelation function Γ_{aoff} accounts for the correlation of speckle after time Δt. Γ_{aoff} approaches zero as $\Delta t >> \tau_{corr}$, the speckle correlation time of the object. In the case of fully correlated speckle ($\Delta t << \tau_{corr}$), $D_{aoff} = 2\sigma_{shot}{}^2$, the shot noise limit.

Similarly, the latter two measurements may be combined:

$$\left\langle \left(a_{on}(t+2\Delta t)-a_{off}(t+\Delta t)\right)^2 \right\rangle = \left\langle \left(a_{off}(t+2\Delta t)+\Delta a_{mm}-a_{off}(t+\Delta t)\right)^2 \right\rangle \approx \overline{\Delta a_{mm}{}^2} + D_{a_{off}}(\Delta t) \tag{2}$$

where the contribution of the induced magnetomotion to the OCT amplitude a is written as Δa_{mm}. If magnetomotion and background fluctuations are uncorrelated, they are separable as shown. We may then write an appropriate expression for the signal S_{mm} in decibels for sensing the presence of magnetomotion:

$$S_{mm} = 10\log\left(\frac{\left\langle \left(a_{on}(t+2\Delta t)-a_{off}(t+\Delta t)\right)^2 \right\rangle + \delta^2}{\left\langle \left(a_{off}(t+\Delta t)-a_{off}(t)\right)^2 \right\rangle + \delta^2}\right) \approx 10\log\left(\frac{\Delta a_{mm}{}^2}{D_{a_{off}}(\Delta t)}+1\right) \tag{3}$$

A small offset δ (typically one bit) is employed to avoid the poles. Because a single 3-point measurement of S_{mm} is excessively noisy, in practice we employ area averaging of spatially over-sampled images. The logarithm term ensures that the mean value of S_{mm} approaches zero in the absence of magnetomotion. As we will demonstrate *in vivo*, this technique is effective at ensuring high specificity to magnetomotion by normalizing against the intrinsic background fluctuations D_{aoff}, which effectively removes biological motion artifacts.

2.2 Physics of MMOCT

There are a number of physical parameters which dictate the mechanics of magnetic particle motion and how it results in optical scattering changes observable with OCT. In brief, we conceptually write the contributions of these parameters to Δa_{mm} as follows:

$$\begin{aligned} \Delta a_{mm}(\vec{r}) &= f\left\{s(\vec{r}), \vec{B}(\vec{r}), \rho(\vec{r}), m_{pp}(\chi_m, M_{sat}, V, H_c), Med(E(\vec{r}), \eta(\vec{r})), b(\vec{r})\right\} \\ &\approx f_s(s(\vec{r}))\cdot f_B(B(\vec{r}))\cdot f_\rho(\rho(\vec{r}))\cdot f_e(\vec{r}) \end{aligned} \tag{4}$$

#8043 - $15.00 USD Received 6 July 2005; revised 15 August 2005; accepted 15 August 2005

where s is the spatially-averaged optical scattering (as measured by averaging the OCT amplitude a over several speckles), $\vec{B}$ is the magnetic field, ρ is the particle concentration, m_{pp} are the relevant magnetic particle properties which include the magnetic susceptibility χ_m, saturation magnetization M_{sat}, volume V, shape, and coercive field H_c, Med are the medium mechanical properties which include the elastic modulus E and viscosity η, and b accounts for the particle-medium interaction such as receptor-ligand binding. In this work we focus on understanding the signal dependence on the object scattering s, magnetic field strength B, and particle concentration ρ, while keeping all other parameters constant (as lumped into f_e). In practice we find that s is unaffected by application of the magnetic field so that f_s and f_B are separable. We expect the local magnetic field to be unaffected by the presence of the low magnetic particle concentrations employed here, allowing separation of f_B and f_ρ. Finally, we will demonstrate in Section 4.2 that for all but the highest magnetic particle concentrations employed, s is unaffected, allowing separation of f_s and f_ρ.

Now, let us track the effect on Δa_{mm} by the applied magnetic field in order to make predictions about the nature of f_ρ, f_B and f_s. All substances are characterized by a magnetic susceptibility $\chi \equiv \partial M/\partial H$, where M is the magnetization and H the applied magnetic field. The magnitude of χ is typically largest when M and H are nearly zero, decreasing as M approaches saturation (M_{sat}). Within a weakly magnetic medium of χ_{med} and M_{med} such as biological tissues, $\mu \approx \mu_0$ and the applied magnetic field $B=H/\mu_0$. In this medium, the force on a small magnetic particle with $\chi=\chi_p$, magnetization M_p, saturation magnetization M_{sat}, and volume V is written $\vec{F}_p = V\left(\left(\vec{M}_p - \vec{M}_{med}\right)\cdot\nabla\right)\vec{B}$. It is useful to consider the following limiting cases [*e.g.*, 20]:

$$\begin{aligned} \vec{F}_p &= \frac{V\left(\chi_p - \chi_{med}\right)\nabla\left|\vec{B}\right|^2}{2\mu_0}, \qquad \left|\vec{M}_p\right| << M_{sat} \\ \vec{F}_p &= VM_{sat}\nabla\left|\vec{B}\right|, \qquad\qquad \left|\vec{M}_{med}\right| << \left|\vec{M}_p\right| = M_{sat} \end{aligned} \tag{5}$$

Note that $\vec{F}_p$ points in the same direction regardless of the polarity of $\vec{B}$.

Here we see that the largest force may be obtained by using materials that exhibit the largest χ and M_{sat}. Although in this work we have used ferromagnetic particles because they exhibit large χ, it is not a necessary condition for Eq. (5). One potential consequence of the use of ferromagnetic particles, however, is that they exhibit remanent magnetization M_{rem}, which results in particle rotation if $\vec{M}_{rem}$ is not aligned with $\vec{B}$, as described by the torque $\vec{\tau} = V\vec{M}_{rem}\times\vec{B}$. For the nanoparticles used in this study, we find no significant difference in the MMOCT signal when premagnetizing ferromagnetic nanoparticle-embedded samples at different angles with respect to $\vec{B}$. We present additional evidence for the dominance of translation versus rotation in Section 4.1.

In the next step, we relate the magnetically-applied force F_p per particle to the resultant displacement Δz of a medium containing a magnetic particle density ρ. For simplicity we will consider magnetic particles bound within a perfectly elastic medium described by Young's modulus E. The reason for this assumption of elasticity is two-fold: because we wish to image particles that are bound with their target molecules, and because the dynamic range of MMOCT is greater when Brownian motion is reduced. Therefore we may neglect the situation of unbound particles in a low viscosity medium. Viscosity does affect the rate of medium deformation, and the implications of this toward imaging speed will be briefly discussed in Section 2.3.

For simplicity let us consider an infinitesimally small cubic volume with sides of length d. Upon application of an upward magnetic field gradient, the top of the cube experiences a total

#8043 - $15.00 USD Received 6 July 2005; revised 15 August 2005; accepted 15 August 2005

magnetic force $F_{tot}=F_p\rho d^3$, where F_p is the force from a single particle (Eq. (5)), ρ is the number density of the magnetic particles, and d^3 the volume of the cube. If the bottom surface of the cube is stationary, the cube elongates so that the top surface is displaced Δz from its original position, as derived using Hooke's law:

$$\Delta z = d\left(\frac{F_{tot}/d^2}{E}\right) = \frac{\rho F_p d^2}{E} \tag{6}$$

The resulting Δz is linear in F_p and ρ, and inversely proportional to E.

As the final step, consider the effect of magnetically-induced particle displacement on the OCT signal change Δa_{mm}. For simplicity, let us consider an individual point-like scattering structure ($d<<w_0$, $d<<l_c$, where d is the particle diameter, w_0 the beam radius, and l_c the coherence length) which is displaced by an adjacent magnetic nanoparticle (with insignificant optical scattering). The locations of the beam and coherence gate (*i.e.*, the imaging location) are $\vec{r}_0(x,y)$ and z_d, respectively (where $\vec{r}$ is the position vector perpendicular to the beam propagation direction). The point scatterer is located at $\vec{r}_p, z_p$. In this situation the OCT signal envelope is equivalent to the envelope of the point spread function which has been previously derived [21]. As demonstrated in Section 4.1 below, typically the structure undergoes a small displacement $\left|\Delta\vec{r}_p\right| << w_0$ and $\Delta z_p << l_c$. Therefore Δa_{mm} may be approximated by differentiation with respect to its position:

$$\Delta a_{mm}\left(\vec{r}_p, z_p; \vec{r}_0, z_d\right) \propto -2a_0\left(\frac{\left(\vec{r}_p-\vec{r}_0\right)\cdot\Delta\vec{r}_p}{{w_0}^2} + 4\ln 2\frac{\left(z_p-z_d\right)\Delta z_p}{{l_c}^2}\right)e^{-\left(\frac{\left|\vec{r}_p-\vec{r}_0\right|}{w_0}\right)^2 - 4\ln 2\left(\frac{z_p-z_d}{l_c}\right)^2} \tag{7}$$

where a_0 is the peak envelope signal. Δa_{mm} has symmetric positive and negative lobes with a single maximum and minimum at $\pm\Delta a_{\max}$ occurring along the axis of displacement at positions $\left(\vec{r}_{0\max}, z_{d\max}\right) = \left(\vec{r}_p \pm \Delta\vec{r}_p/\xi, z_p \pm \Delta z_p/\xi\right)$, respectively, where:

$$\Delta a_{\max} = \sqrt{2}a_0\sqrt{\frac{\left|\Delta\vec{r}_p\right|^2}{{w_0}^2} + 4\ln 2\frac{{\Delta z_p}^2}{{l_c}^2}} = \sqrt{2}a_0\xi \tag{8}$$

We see that $\Delta a_{\max}$ increases linearly with ξ, the magnitude of displacement in a Cartesian coordinate system scaled by the optical resolution.

In practice, Δa_{mm} is sampled over a speckled region composed of many subresolution scatterers. The overall response in this situation depends the movement of each scatterer within the coherence volume, because speckle arises from the superposition of the scattered field from each particle and its interference with the reference field. Using homogenous tissue phantoms we have found qualitatively that the speckles displace without significant change in their overall structure, suggesting that the relative positions of the subresolution particles remain fixed. In this case it is straightforward to observe that by averaging over the probability density function of a over multiple speckles [22], the scaling of Δa_{mm} with a_0 and ξ is conceptually the same for the single- and multiple-scatterer case. However, in the multiple-scatterer case it is necessary to define a new parameter s to describe the average signal (proportional to the average of a_0) over multiple speckles.

#8043 - $15.00 USD Received 6 July 2005; revised 15 August 2005; accepted 15 August 2005

Putting the above concepts together (Eqs. (5-8)) it is possible to predict the forms of f_ρ, f_B and f_s of Eq. (4) for a homogenous sample. This is written in terms of a power-law dependence on each variable:

$$\begin{aligned} \Delta a_{mm} &= f_s \cdot f_B \cdot f_\rho \cdot f_e \\ &\propto s^{n_s} B^{n_B} \rho^{n_\rho} \end{aligned} \tag{9}$$

where the above development predicts n_ρ=1, n_B=1 in saturation and n_B=2 below saturation, and n_s=1. Experiments were performed to measure these power dependencies, as described below.

2.3 Imaging System Design Considerations

The choice of sampling rate ($1/\Delta t$) is subject to a number of considerations. Reduction of Δt is desired to minimize speckle noise (Eq. (1)). For example, in chicken skin the speckle correlation time τ_{corr} is approximately 100 ms [23]. However, this reduction is limited by the time necessary for the medium to complete magnetomotion both during and after application of the magnetic field (otherwise the measured Δa_{mm} will be smaller). This equilibriating time, proportional to the medium property η/E, was found to be <1 ms in the tissue phantoms described below. Another limitation to the sampling rate may be inductive heating. Hyperthermia induced by modulation of magnetic particles has been used for therapeutic purposes such as selective tissue or cell lysis [24], and is generally found to be significant at frequencies above 100 kHz. Finally, magnetic field modulation at higher frequencies requires thoughtful design of the electromagnet because the inductance becomes prohibitive.

Electromagnet design should take into account the fact that, for OCT, the imaging volume is typically small (~2 mm on a side) and for *in vivo* imaging the tissue is relatively thick with respect to the imaging space. Since electromagnet power is used more efficiently by placing it as close as possible to the imaging volume, a simple solenoid coil placed on top of the tissue or encircling the imaging objective is appropriate. The magnetic field gradient in the direction along the coil axis is maximized by reducing the inner coil radius, and the central bore is used for passage of the OCT imaging beam to the tissue [18]. Particle displacement in these experiments is therefore primarily in the axial direction when imaging through the center of the coil.

There are many valid design options for synchronizing the magnetic field application with the image acquisition. In one implementation [25] a lock-in amplifier was used to detect magnetic-specific modulation at 1 kHz, collecting data separately at each point within the OCT image. However, this type of imaging sequence is prohibitively long. The technique described below synchronizes the magnetic field application with the axial scan line acquisition. This allows for sampling rates from 10 Hz for the high sensitivity system described here, to >10 kHz for spectral-domain OCT systems [26].

3. Experimental Materials and Methods

3.1 Magnetomotive Optical System

The OCT system used in this investigation is depicted in Fig. 1. A femtosecond Ti:Al_2O_3 laser (KMLabs, Inc.) light source with typically a 120 nm bandwidth centered at 800 nm (providing l_c=3 μm axial resolution) was pumped with 4.5 W from a frequency-doubled (λ=532 nm) Nd:YVO_4 laser (Coherent, Inc.). This source light was launched into a single-mode fiber interferometer and provided 5 mW (phantoms study) or 10 mW (*in vivo* study) of light power at the sample. The collimated sample light is scanned laterally using galvanometer-mounted mirrors and directed through a 40 mm (phantoms study) or 20 mm (*in vivo* study and high-resolution phantoms) focal length achromatic lens, providing $2w_0$=16 or 8 μm lateral resolution, respectively. Optical delay is provided at a repetition rate of 10 Hz by directing collimated light from the reference arm of the interferometer into a galvanometer-

#8043 - $15.00 USD Received 6 July 2005; revised 15 August 2005; accepted 15 August 2005

mounted retroreflector. Noise from the source light is subtracted from the OCT signal at a dual-balanced photodetector (Nirvana, New Focus, Inc.), and the resulting signal is simultaneously digitally bandpass filtered and rectified via the Hilbert transform. In practice, this bandpass filter did not exclude the Doppler-shifted signal arising from potentially moving magnetic particles in the samples discussed below, although it should be noted that pure liquid samples exhibited large Doppler shifts. The sensitivity of this system is –101 dB when compared to the signal from a mirror placed in the sample arm.

For this work we constructed a small, water-jacketed solenoid with a 1 cm diameter bore, an outer diameter of 18 mm, and an axial thickness of 9 mm. Operated at 100 W, the electromagnet delivers an axial magnetic field B=0.06±0.01 T and axial magnetic field gradients of $\nabla|B|$=11±1 T/m and $\nabla|B|^2$=1.3±0.4 T^2/m, where errors indicate the deviation expected over a 2 mm imaging volume. The bottom surface of the coil jacket was positioned ~0.5 mm above the top surface of the sample object. A computer-controlled power supply switched current to the electromagnet during acquisition of the axial scan lines (see inset of Fig. 1) such that $a_{off}(t)$, $a_{off}(t+\Delta t)$, and $a_{on}(t+2\Delta t)$, (Δt=100ms) were acquired successively at each lateral position. The timing was adjusted such that the coil switching occurred in the rest periods between line acquisition, allowing sufficient buffer time (>1 ms) for the particles to complete movement.

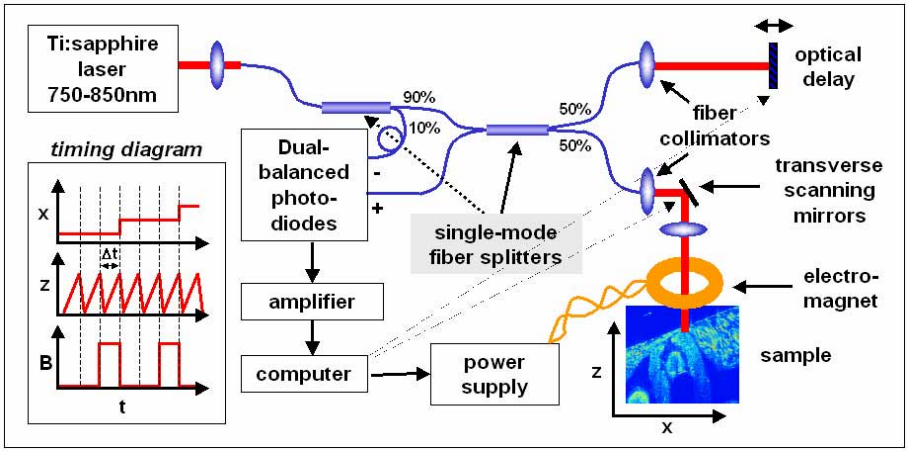

Fig. 1. Diagram of the MMOCT system. Synchronization of image acquisition in x and z with the modulation of the magnetic field B is illustrated in the timing diagram (lower left inset).

3.2 Magnetic Particle Properties

Magnetite ($Fe_3^{(II,III)}O_4$) nanoparticles nominally 20-30 nm in size (Sigma-Aldrich, #637106) were used in all experiments detailed below. Their magnetic characteristics were determined using SQUID (superconducting quantum interference device) magnetometry (MPMS, Quantum Design, Inc.) The M=0, H=0 volume susceptibility was χ_p=2.9. The volume magnetization at B=0.06 T was M_p=125 kA/m, and the saturation magnetization was M_{sat}=203 kA/m, suggesting that the particles may be nearly, but not completely, saturated at the maximum magnetic field strength employed in these experiments. Evidence of ferromagnetism was also noted, with M_{rem}=19 kA/m at H=0 and coercive field H_c=0.0063 T. Using Eq. (5), the magnetic force per particle is computed to be $F_p(0.06T)=1.9\cdot10^{-17}$ N. This apparently small number should be weighted against the small size of the nanoparticles and the fact that we detect their cooperative effect. For example, a 1 μm spherical total volume of particles exerts a total force F_{tot}=5.7 pN.

#8043 - $15.00 USD Received 6 July 2005; revised 15 August 2005; accepted 15 August 2005

3.3 Tissue Phantom Preparation & Measurements

Tissue phantoms were constructed to simulate both the optical scattering and the elastic properties of tissue. Silicone-based phantoms were employed due to the ability to adjust their elasticity by balancing the mixture of polymers. The polymer ratios used here were determined by qualitatively comparing phantom mechanical properties to soft human tissue. A silicone solution was prepared consisting of 90.4% pure polydimethylsiloxane (PDMS) fluid (50 cSt viscosity, ClearCo, Inc.), 8.8% specialty PMDS and 0.8% PDMS curing agent (General Electric RTV-615A and B, respectively, Circuit Specialists, Inc.) To approximate the optical response of tissue as imaged with OCT, TiO_2 microparticles (Sigma-Aldrich, #224227, mean size 1 μm, <5 μm) were added at a concentration of 4.1 μg/g to the silicone mixture. This concentration was chosen by comparing TiO_2-doped phantoms of varying concentration to 2% intralipid (which is known to be representative of human skin [27]). In particular, the TiO_2 concentration was adjusted to match the peak OCT signal and depth attenuation of the intralipid. It should be noted that the addition of particles tended to increase the elastic modulus of the phantom, thus polymer mixture balancing was performed after addition of TiO_2.

A set of phantoms with varying magnetic particle concentration was prepared by adding ρ=0, 32, 63, 120, 220, 450, 930, 2600, and 5400 μg/g magnetite nanoparticles to the silicone/TiO_2 stock solution and sonicating each sample >5 hours at <25°C. Each sample was poured into a 35 mm cell culture dish cover, cured overnight at 70°C, and cured an additional 24 hours at room temperature. Each sample weighed >10 g to ensure the mechanical response was similar to bulk tissue. There was no palpable difference in the elastic modulus of the samples. Another set of phantoms were prepared identically, except with only 30 minutes of sonication, resulting in an inhomogeneous dispersion and precipitation. Two of these were used in the magnetic field dependence study of Fig. 3; their actual concentrations were estimated by mass spectrometry as sampled from the top portion of the phantom.

All OCT images were sampled at 600 × 1000 pixels laterally and axially, respectively, resulting in an image acquisition time of 1 minute. Because three columns are required for each MMOCT measurement, this resulted in 200 MMOCT pixels laterally. For the high-resolution cross-correlation data (Fig. 2) the uncropped physical image size was 180 × 200 μm. For all other phantom data, images were acquired over 600 × 700 μm. $\Delta a_{mm}{}^2$ was determined using the relation:

$$\Delta a_{mm}{}^2 = \left\langle \left(a_{on}(t+2\Delta t) - a_{off}(t+\Delta t)\right)^2 \right\rangle - \left\langle \left(a_{off}(t+\Delta t) - a_{off}(t)\right)^2 \right\rangle \tag{10}$$

which combines Eqs. 1 and 2. Because the measurement of $\Delta a_{mm}{}^2$ often results in negative values, the fits of experimental data have been carried out on the square of $s^{n_s} B^{n_B} \rho^{n_\rho}$ (from Eq. (9)).

3.4 In Vivo Measurements

Twenty-four hours prior to imaging, African frog tadpoles (*Xenopus laevis*) 5 weeks of age were placed into a tank with food and with ~ 1 mg/mL magnetic nanoparticles. In this study, one control and one magnetite-exposed tadpole were anaesthetized by immersion in 0.05% tricaine for 2 minutes, and subsequently imaged with MMOCT while immersed in a more diluted (~0.005%) solution of tricaine. MMOCT images were acquired from varying locations by aligning the long-axis of the tadpole with the lateral scanning direction (the sagittal plane), and imaging from both the dorsal or ventral sides. Images were sampled at 600 × 1000 pixels over a 2 mm × 1.5 mm region laterally and axially, respectively. None of the control tadpole images exhibited significant magnetic signal S_{mm}. Tadpoles were subsequently euthanized by long exposures to 0.05% tricaine (> 10 minutes) and preserved in 10% formalin for subsequent histology. In previous experiments under similar conditions,

#8043 - $15.00 USD Received 6 July 2005; revised 15 August 2005; accepted 15 August 2005

magnetite-exposed tadpoles (n>5) were revived after imaging and survived > 48 hours. Tissues were microtomed in the same plane as the OCT images, and stained for iron (HT-20 Kit, Sigma).

4. Results and Discussion

4.1 The Mechanics of Magnetomotion

By over-sampling high resolution OCT images during magnetic field modulation, we gain insight into the nature of magnetic nanoparticle induced motion. The image in Fig. 2 illustrates the line-by-line acquisition of $a_{off}(t)$, $a_{off}(t+\Delta t)$, and $a_{on}(t+2\Delta t)$ in the 0.93 mg/g magnetite-doped tissue phantom. The axial displacement of the TiO_2 microparticle optical scatterers is observed in the third column corresponding to a_{on} at each lateral position. The amplitude of the axial and transverse displacements over the homogenous phantom is measured using a cross-correlation algorithm developed previously for OCT [28]. Using this, the displacement vector for pixels above a 1% threshold was assigned the maximum value of the normalized cross-correlation within a 10 × 10 μm window, (which assumes the displacement magnitudes are ≤ 5 μm). Histograms of the axial (Δz) and lateral (Δx) displacements for this phantom are displayed on the bottom of Fig. 2. Due to hardware positioning limitations the lateral sampling size was larger than the axial. (It should also be noted that, due to the pancake-shaped resolution volume of the OCT system, MMOCT is $w_0\sqrt{(4\ln 2)}/l_c \sim 4\times$ less sensitive to lateral movement via Eq. (8)). We found that the lateral displacement was undetectable at this resolution, placing an upper bound of 500 nm on its magnitude. In contrast, the axial displacement is clearly seen as a peak in the histogram at +200 nm (upwards), resulting in a population averaged Δz=130 nm. Although this data does not exclude the possibility of lateral motion, at higher particle concentration (ρ=5.4 mg/g) with larger (and possibly saturated) motion we found $\langle\Delta z\rangle/\langle\Delta x\rangle$ = 3.5 and therefore we expect the dominant contribution to the MMOCT signal is Δz by a factor of ~14.

Since the particles are ferromagnetic there may exist a torque upon application of B. One possible consequence is that the particles will align with their long axes along B=B_z, resulting in a reduction of the physical cross-section seen along z and thus reduction of optical scattering from the particles. This effect was observed for unbound nanoparticles in water under a light microscope. (In the phantoms this would be observed at high ρ where the optical effect of the nanoparticles becomes observable, as discussed below). This rotational effect would manifest as an anisotropy in $\Delta a_{on/off} = a_{on}(t+2\Delta t)-a_{off}(t+\Delta t)$. A histogram of the $\Delta a_{on/off}$ values for the sample of Fig. 2 is shown. It is symmetric about $\Delta a_{on/off}$=0, suggesting that the above proposed rotational mechanism is not significant here. All images acquired in this study have also been found to exhibit a symmetric response for $\Delta a_{on/off}$.

The scaling of Δa_{mm} with the magnitude of B was investigated in tissue phantoms at three concentrations, as shown in Fig. 3. The magnitude of B was determined by the electromagnet voltage during acquisition of a_{on}. One image at each value of B was acquired, using a random sequence of B values to reduce the effect of long time scale drift. The resulting $\Delta a_{mm}{}^2$ values (Eq. (10)) were averaged over the phantom area and are plotted in Fig. 3, where they have been least-squares fitted to the power-law scaling model of Eq. (9). The best fit values of n_B between 1.41 and 1.47 suggest behavior that is in between the limiting cases of Eq. (5). This is reasonable considering the SQUID measurements indicate the magnetization of the nanoparticles at approximately half their saturation magnetization at B=0.06 T. Further investigation may reveal whether the slight increase of n_B with concentration is significant.

#8043 - $15.00 USD Received 6 July 2005; revised 15 August 2005; accepted 15 August 2005

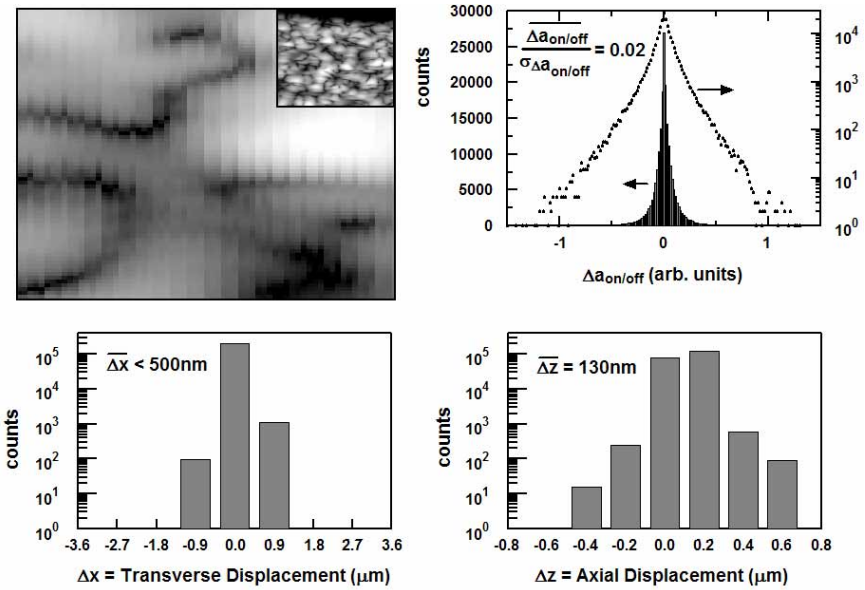

Fig. 2. Mechanics of MMOCT. Upper left: Closeup of MMOCT image (20 × 15 μm) of a tissue phantom (ρ=0.93 mg/g), inset a larger view (110 × 90 μm). Upper right: Histogram of $\Delta a_{on/off}$ values from phantom image in linear (left) and log (right) scales as indicated by the arrows. Lower panels: Log histograms of lateral (Δx) and axial (Δz) displacements from above image.

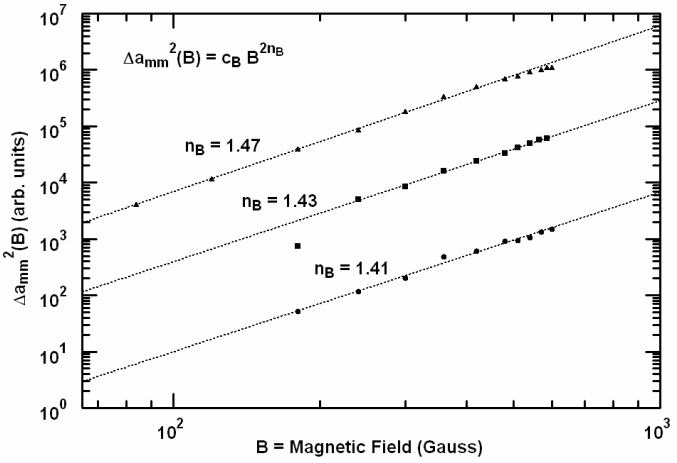

Fig 3. Magnetic field dependence of Δa_{mm}^2 in tissue phantoms. Triangles: ρ~1.2 mg/g. Squares: ρ~0.77 mg/g. Circles: ρ=0.45 mg/g. The best fits to the model are plotted as dotted lines.

As shown in Fig. 4, the dependence of Δa_{mm} on the concentration of magnetite particles ρ nearly follows a linear power law (n_ρ=1.1), as predicted in the above development. The following section includes further discussion on imaging quality versus ρ.

The dependence of Δa_{mm} on the speckle-averaged OCT signal s was investigated. The phantoms were sufficiently homogenous such that s was well-described as purely a function of image depth z. The average value of s and Δa_{mm} at each depth was evaluated for the same image set reported in Fig. 4. However, in order to compare the responses from different

#8043 - $15.00 USD Received 6 July 2005; revised 15 August 2005; accepted 15 August 2005

depths, correction for the depth-dependence of B, $f_B(z)$, was performed by acquiring images of the same sample for various displacements of the electromagnet away from the sample. In this way, a monotonically decreasing function for $f_B(z)$ was determined and fit to a second order polynomial, as plotted in Fig. 5. We see that the dropoff of f_B is approximately 32% per millimeters of imaging depth, which is consistent with the predicted dropoff of $\nabla|B|^2$ of 28%/mm, within experimental error. In Fig. 5 we plot the depth-dependent functions Δa_{mm}^2, s and f_B for a representative image of a tissue phantom. The predicted z-dependence of $\Delta a_{mm}^2 = f_B^2 s^{2ns}$ (n_s=1) appears to very closely match that of Δa_{mm}^2, with the primary difference observed for the low values of Δa_{mm}^2 at large z. This may be due to shot noise contributions which were not accounted for.

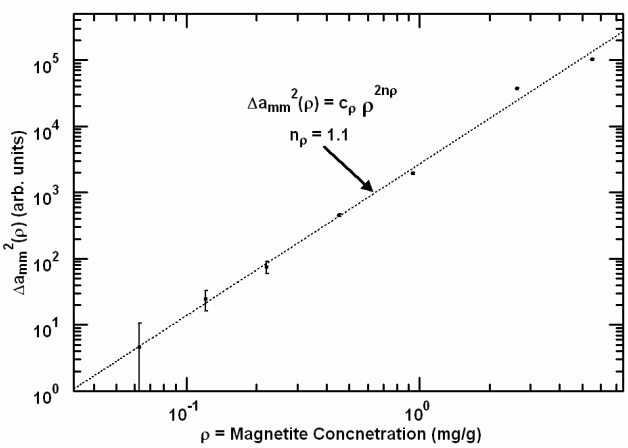

Fig 4. Magnetic nanoparticle concentration dependence of Δa_{mm}^2 in homogenous tissue phantoms. At each concentration, 4 or more images were acquired in different locations. The mean and standard deviation of the image-averaged Δa_{mm}^2 is plotted.

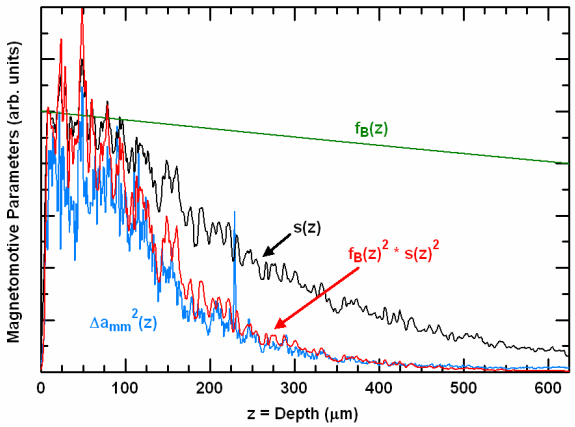

Fig. 5. Depth-dependent functions Δa_{mm}^2, s, f_B, and the $f_B^2 s^2$ prediction of Δa_{mm}^2 are indicated, as averaged laterally across a tissue phantom MMOCT image (ρ=0.93 mg/g). All functions have been scaled separately for the purposes of comparison.

To more precisely determine the value of n_s (Eq. (9)) we plot $\Delta a_{mm}^2/f_B^2$ (which should equal f_s^2) versus s in Fig. 6. The scatter data suggest a nearly linear scaling of Δa_{mm} with s (n_s=0.87-0.97), which is consistent with the above predictions. The apparent thresholding

#8043 - $15.00 USD Received 6 July 2005; revised 15 August 2005; accepted 15 August 2005

behavior for low Δa_{mm} warrants further investigation. It is also not clear whether the slight increase in n_s with ρ is significant.

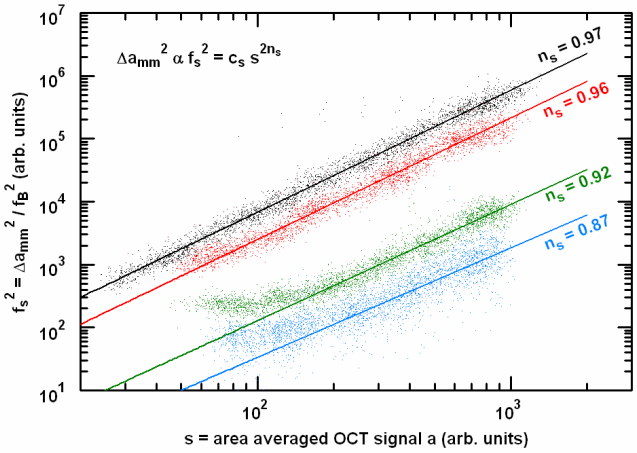

Fig. 6. Scatter plot of f_s^2 versus s for image sets acquired in tissue phantoms at four concentrations. Black: ρ=5.4 mg/g, red: ρ=2.6 mg/g, green: ρ=0.93 mg/g, and blue: ρ=0.45 mg/g. The associated best fit lines which were fit to data points above the apparent "knee" are drawn.

4.2 MMOCT Imaging Qualities

To this point in the paper we have achieved an understanding of some of the underlying mechanisms that dictate the magnetic-specific change in the OCT amplitude Δa_{mm}. The ability to sense the locations of magnetic nanoparticles in tissue for imaging purposes, however, is determined by the size of Δa_{mm} relative to the background fluctuations D_{aoff}, as quantified by the parameter S_{mm} of Eq. (3). One consequence is that, despite the rapid falloff in Δa_{mm} with image depth (Fig. 5), the falloff in S_{mm} is actually very gradual. This can be understood by the fact that D_{aoff}, like Δa_{mm}^2, scales with the square of the OCT signal amplitude (Eq. (1)) when it is significantly above the shot noise level. The depth-dependent falloffs of these functions are displayed in Fig. 7.

It is also interesting to compute the average value of S_{mm} for the concentration-dependent data, in order to rate the confidence with which the presence of magnetic particles may be identified. We summarize the values of S_{mm} for smaller ρ in Table 1. The t-value was computed against data from the control tissue phantom (ρ=0), and the resulting number of images n necessary to reach a confidence > 97.5% by the t-test is reported. This suggests that this system is able to detect 220 μg/g magnetite nanoparticles when averaging over 3 images. However, it should also be noted that sufficient statistics (n>10) to accurately apply the t-test were not acquired here (n≥4), and thus the result that concentrations down to 63 μg/g had t-values on the order of 1 may suggest the possibility of achieving even better sensitivity with more sampling, or with minor improvements in the MMOCT system.

Another important imaging parameter is the maximum possible dynamic range, which equals the value of S_{mm} corresponding to 100% amplitude modulation. This was computed from the image data of the tissue phantoms at each concentration, and was found to be 27 dB, with a slight falloff observed for ρ=2.6 and 5.4 mg/g to 25 and 24 dB, respectively. By analyzing the depth-dependence of $s(z)$ we determined this falloff is due to increased absorption in the sample arising from the nanoparticles themselves. In comparison, the maximum achieved S_{mm} value (ρ=5.4 mg/g) was 18 dB, which corresponds to an average amplitude modulation of ~30%. Given the random nature of speckle, we expect 18 dB is

#8043 - $15.00 USD Received 6 July 2005; revised 15 August 2005; accepted 15 August 2005

likely a practical upper limit on the dynamic range for this system for densely scattering tissue-like media. However, one should weigh this against the extremely low mean and standard deviation exhibited in the value of S_{mm} for the control sample which was only –0.017±0.075 dB. Given this small standard deviation, it is possible to evaluate S_{mm} with sufficient accuracy for imaging by averaging over smaller areas than those employed above (600 × 700 μm). In fact, this was performed in the *in vivo* experiment to follow, in which S_{mm} is median filtered over 40 × 30 μm (lateral × axial) to produce the MMOCT image.

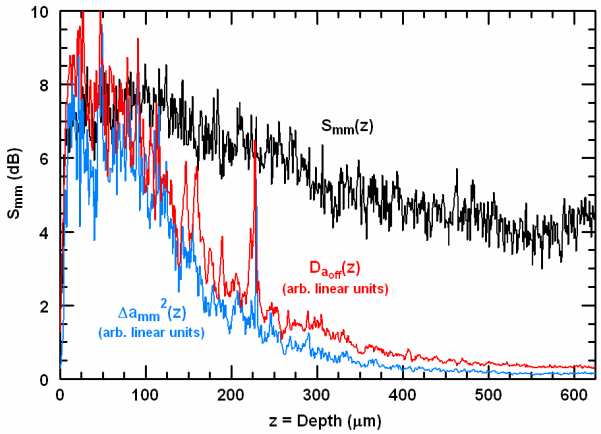

Fig. 7. Depth-dependence of Δa_{mm}^2, D_{aoff}, and S_{mm} for a representative image of a tissue phantom (ρ=0.93 mg/g). D_{aoff} and Δa_{mm}^2 are plotted on a linear scale and are scaled separately for the purposes of comparison (their relative strengths may be determined by S_{mm}).

Table 1: Magnetic nanoparticle concentration-dependence ρ of the image-averaged values of S_{mm} (shown as S in table), the t-value, and the number of images necessary to achieve the desired sensitivity.

$\rho(\mu g/g)$	$S(\rho)$ (dB)	$\frac{S(\rho)-S(0)}{\sigma_{\Delta S}}$	# images P>.975
0	-0.02	-	-
32	-0.01	0.07	-
63	0.05	0.77	-
120	0.07	1.0	-
220	0.24	2.8	3
450	2.0	24	1

4.3 In Vivo MMOCT

In the above treatment we have laid groundwork for understanding the physical basis of magnetomotive optical contrast, and the characteristics of the background normalized magnetic specific signal S_{mm} relevant to tissue-like samples. In this section, we wish to motivate this work by demonstrating how a spatial measurement of S_{mm} may be represented as a magnetic-specific, MMOCT image. The emphasis in this study is to show the *in vivo* feasibility of the technique, leaving quantification of the imaging resolution and other factors relevant to inhomogeneous samples for future study.

As detailed in Section 3.4, a *Xenopus laevis* (African frog) tadpole was exposed overnight to magnetic nanoparticles in its tank water. The nanoparticles do not disperse well in water, resulting in nominally micron-sized aggregates. It is expected that these aggregates will be taken up by the tadpole suction feeders [29]. Feeding in tadpoles is accomplished by gill rakers which are mucus-coated and which move trapped particles toward the pharynx and

#8043 - $15.00 USD Received 6 July 2005; revised 15 August 2005; accepted 15 August 2005

esophagus. Thus, we expect to see magnetic nanoparticles localized in the gills and digestive tract.

The resulting MMOCT images at varying locations within the magnetite-exposed tadpole are displayed in Figs. 8 and 9. We display the structural OCT data $a(x,z)$, which is the average of $a_{off}(t)$ and $a_{off}(t+\Delta t)$ in the red channel, and the MMOCT data $S_{mm}(x,z)$ in the green channel. Using subsequent histology and literature [30] to aid in the identification of the tadpole anatomy, we discuss the points of apparently significant MMOCT signal (green regions). In Fig. 8, the most striking feature is labeled (c), which is in the region of the intestines. Unfortunately, the surface of the digestive tract is highly scattering which reduces the light penetration in this region. It is interesting to note that adjacent features, such as the tail (to the left), and the heart (d) have no apparent MMOCT signal. It is particularly interesting that the beating heart (d) which exhibits a striped pattern in the structural OCT image due to its movement, does not exhibit appreciable MMOCT signal, which emphasizes the background subtraction nature of this technique. Also in Fig. 8 we observe some MMOCT signal from the tail (a) and molding clay situated underneath the tadpole (b). The movement of the tail might be explained by the fact that it was not sufficiently anchored and thus modulated in response to mechanical coupling with the nearby digestive tract. It is also possible that the tadpole excreted magnetic particles during the course of imaging which were deposited in the molding clay in this region. However, this warrants further investigation.

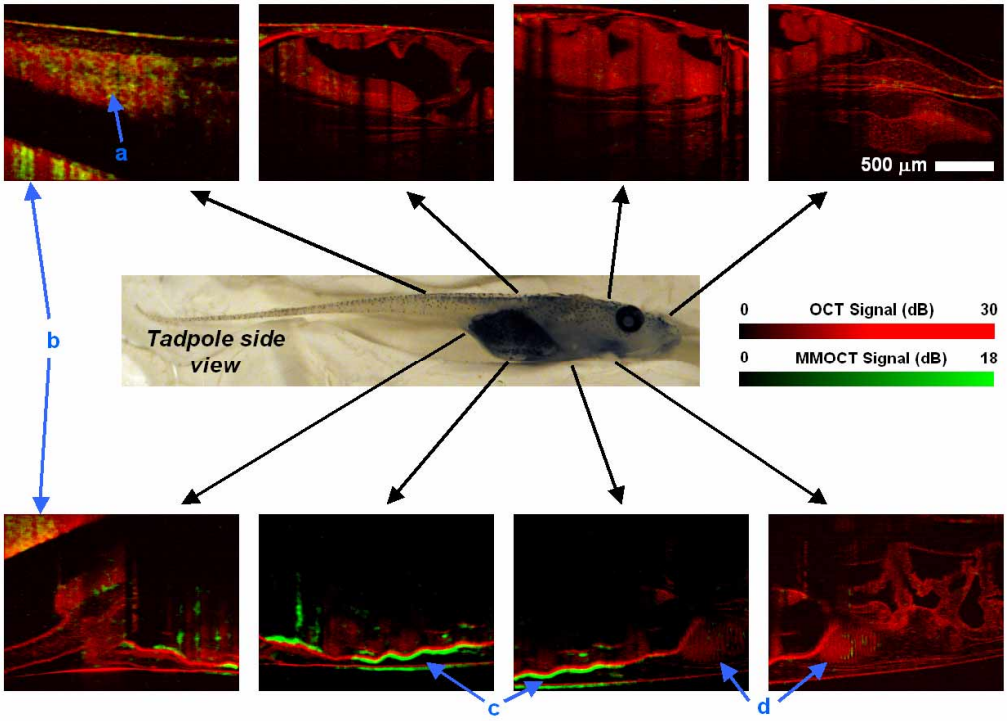

Fig. 8. MMOCT images of magnetic nanoparticle-exposed *Xenopus laevis* tadpole in a single sagittal plane. Approximate image locations are referenced against a microscopy image of a different tadpole of the same age. Points of interest (a-d) are discussed in the text. Scale bars indicate structural OCT (red) and MMOCT (green) scaling displayed in the images.

In Fig. 9, MMOCT images are displayed of sagittal planes displaced from the center of the tadpole. A few regions (e-g) of potentially significant MMOCT signal warrant discussion. Region (e) is part of the central nervous system (brain). Although it might be possible that the pharynx cavity is situated nearby and below the apparent green region (*e.g.* in the bottom left corner of the image), it is not easily explained why this region would exhibit MMOCT signal

#8043 - $15.00 USD Received 6 July 2005; revised 15 August 2005; accepted 15 August 2005

given our present understanding. Region (f) is associated with the front part of the intestine, which occupies a large fraction of the tadpole volume. Region (g) is understood to be a gill structure within the bronchial cavity. Additional gill structures in the image immediately to the left, however, do not exhibit significant magnetomotion.

Subsequent histology was performed by fixation and sectioning of the control and magnetite-exposed tadpole tissues in the same plane as MMOCT images. Slices 10 μm thick were obtained every 100 μm and were stained with Prussian Blue such that iron appears blue, nuclei appear red, and cytoplasm appears pink. All slides were investigated thoroughly for evidence of magnetic particles or endogenous structures which have a similar appearance to magnetic particles. As shown in Fig. 10, melanophores present in both the control and magnetite-exposed tadpole are similar in appearance to magnetic particles. Upon close inspection, however, the lack of a blue halo in the immediate vicinity of the melanin, in addition to its fine granular texture, are distinguishing features which permit differentiation of the two. The appearance of melanophores around the digestive tract explains the poor depth penetration of the MMOCT images in this region. Magnetic nanoparticles were clearly observed throughout the intestines of the magnetite-exposed tadpole as illustrated in a representative histological section in Fig. 10. In other regions, nanoparticles were not observed, even in regions in which they would be expected such as the gills, pharynx, or esophagus. It is not clear, however, whether small quantities of magnetic nanoparticles will remain adhered to the tissue and the slide after the extensive tissue processing and staining, and thus the lack of positive results in these regions is not conclusive.

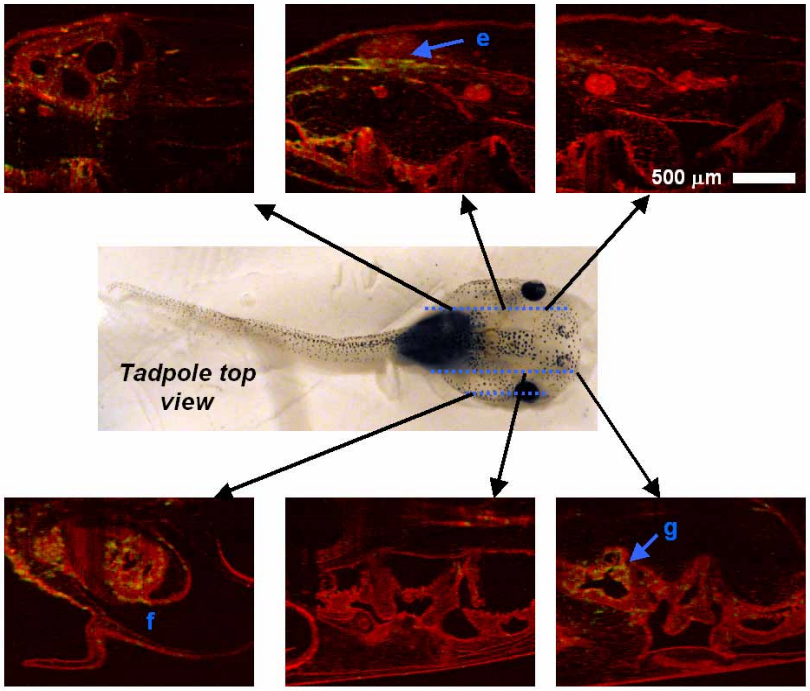

Fig. 9. MMOCT images of magnetic nanoparticle-exposed *Xenopus laevis* tadpole in sagittal planes displaced as shown qualitatively against a microscopy image of a different tadpole of the same age. Points of interest (e-g) are discussed in the text. Color scales are identical to those used in Fig. 9.

#8043 - $15.00 USD Received 6 July 2005; revised 15 August 2005; accepted 15 August 2005

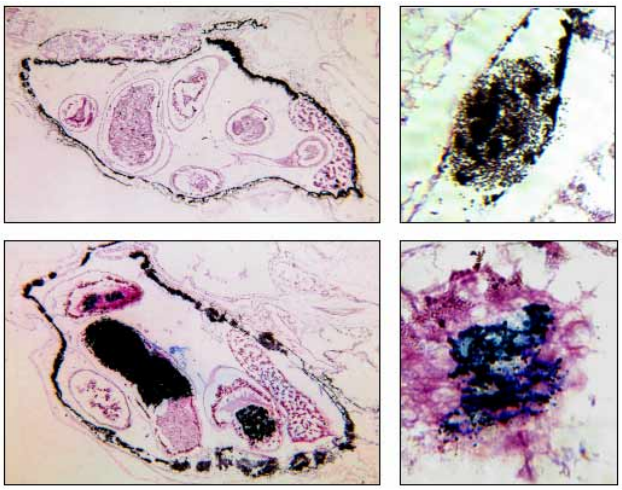

Fig. 10. Histological slices of a control tadpole (top row), and the magnetite-exposed tadpole (bottom row) from Figs. 8-9. Left column: 1.6 × 1.1 mm images of the tadpole digestive tract illustrating bordering melanophores (both) and ingested magnetic nanoparticles (bottom). Right column: 110 × 110 μm magnified regions of dark particles illustrating melanin (top) and magnetic nanoparticles (bottom) which are distinguished by a Prussian blue-stained halo.

Most of the areas exhibiting magnetomotion in Figs. 8 and 9 correspond to regions in the tadpole that might be expected to contain magnetic nanoparticles, with the exception of the brain region (e) in Fig. 9. Although many of these did not appear in the subsequent histology, the most significant region (c) with highest MMOCT signal from the digestive tract clearly corresponds to the histological findings. The fact that the structures immediately surrounding (c) did not exhibit significant magnetomotive signal, and the fact that moving structures such as the heart did not give rise to false positives, illustrate the future potential of MMOCT as an *in vivo* imaging technology.

5. Summary and Conclusion

In summary, we have described a novel magnetomotive imaging technique that uses OCT to measure magnetic-specific optical scattering changes with reference to intrinsic background fluctuations in the specimen. This work demonstrates clearly that MMOCT contrast provides a high background-rejection mechanism for distinguishing magnetic nanoparticles within highly-scattering tissues. This has application toward imaging magnetic nanoparticles as an *in vivo* contrast agent, analogous to MRI [16]. It should also be possible to target the nanoparticles for specific cell receptors to accomplish molecularly-sensitive OCT.

The mechanics of the magnetically-induced optical scattering change are well-explained by the magnetic gradient force exerted on magnetic nanoparticles, elastic deformation of the medium, and subsequent displacement of the speckled structure within the OCT image. Experiments measuring the power-law scaling of the OCT amplitude change with the magnetic field strength, average scattering signal, and concentration of particles are in excellent agreement with predictions. In fact, these results demonstrate the high quality of magnetomotive measurements that can be obtained with OCT and suggest potential future application of OCT for studying the physics of magnetomotion.

Using optically and mechanically correct tissue phantoms, we demonstrated an imaging sensitivity to 220 μg/g of magnetite nanoparticles. The marginal *t*-values for smaller particle concentrations (*e.g.* 0.77 at 63 μg/g), however, suggest that even greater sensitivity may be possible with minor improvements in the imaging apparatus. Such improvements include increasing the image acquisition rate to increase the speckle correlation between measurements through the use of fast scanning hardware such as spectral domain OCT [26]. The depth penetration of MMOCT appears to be restricted only by the penetration of the OCT

#8043 - $15.00 USD Received 6 July 2005; revised 15 August 2005; accepted 15 August 2005

images to the point where the return signal is no longer significantly above the shot noise, and in fact the falloff in depth of the MMOCT signal is more gradual than that of the OCT signal itself. Future study is needed to understand the response from heterogeneous samples and the dependence on tissue viscoelasticity, and to measure the imaging resolution of the MMOCT signal.

In vivo MMOCT contrast is observed in *Xenopus laevis* tadpoles using concentrations of iron oxide that were well-tolerated and non-toxic. In fact, MMOCT correctly identified the region of largest nanoparticle concentration in the digestive tract of the tadpole, as verified with corresponding histology. The fact that there were additional, weaker regions of MMOCT signal not seen in the histology is an area of future investigation, since histology may not preserve small concentrations of particles through the extensive tissue fixation and staining process. Finally, physiological movement such as the beating of the tadpole heart was fully rejected by this novel three-measurement technique which normalizes against the background.

These promising results set the stage for future progress in molecular OCT imaging. The utility of MMOCT as a molecular imaging tool will only be realized when agents are surface-modified to target cells and disease with high specificity. The availability of FDA-approved MRI contrast agents with similar properties to those employed here may be an ideal starting point for future investigations.

Acknowledgments

We acknowledge Wei Luo, Dr. Daniel Marks, Prof. Scott Carney, and Prof. Andrew Webb from the University of Illinois at Urbana-Champaign for their technical assistance, helpful discussions, and equipment. All animals used in these studies were handled and cared for according to protocols approved by the Institutional Animal Care and Use Committee of the University of Illinois at Urbana-Champaign. This research was supported in part by The Whitaker Foundation (RG-01-0179, S.A.B.), the National Institutes of Health (1-R01-EB001777-01, A.W., S.A.B., and 1-R01-HL25934, K.S.S.), and the NSF (CHE-03-15494, K.S.S.)

#8043 - $15.00 USD Received 6 July 2005; revised 15 August 2005; accepted 15 August 2005